Supporting information

Ultra-high performance of ionic thermoelectric-electrochemical gel cells for harvesting low grade heat

Yong-Bin Zhu[a,‡], Cheng-Gong Han[a,‡,*], Jiawei Chen[a], Lijuan Yang[a], Yingming Ma[a], Hongyu Guan[a], Dongxue Han[a], Li Niu[a,b,*]

1. Center for Advanced Analytical Science, Guangzhou Key Laboratory of Sensing Materials and Devices, Guangdong Engineering Technology Research Center for Photoelectric Sensing Materials and Devices, Key Laboratory of Optoelectronic Materials and Sensors in Guangdong Provincial Universities, School of Chemistry and Chemical Engineering, Guangzhou University, Guangzhou 510006, P. R. China.
2. School of Chemical Engineering and Technology, Sun Yat-Sen University, Zhuhai 519000, P. R. China.

‡ These authors contributed equally to this work.

*Corresponding Email: hancg@gzhu.edu.cn (Cheng-Gong Han); lniu@gzhu.edu.cn (Li Niu)

Note 1. Measurement of electrode temperature coefficient

The determination for electrode temperature coefficient is based on a three-electrode system, where Pt and saturated calomel electrode (SCE) are inserted into gels G-*m/n* $FeCN^{4-/3-}$ and G-*x/y* I^-/I_3^-, serving as the working electrode, reference and counter electrodes, respectively. The gels system in a water bath is slowly heated, and an electrochemical working station is used to collect the voltage vs. SCE per 1 K intervals in the temperature range of 293-343 K. The slop of voltage vs. temperature corresponds to the electrode temperature coefficient $\alpha_{R\ vs\ SCE}$ of gels, i.e., $\alpha_R = \alpha_{R\ vs\ SCE} + \alpha_{SCE}$, where α_R is the absolute electrode temperature coefficient, and α_{SCE} is the electrode temperature coefficient of SCE ($\alpha_{SCE} \approx -0.47\ mV^{-1}$).[S1]

Note 2. Determination of ionic thermopower for i-TE gels cell

For the thermodiffusion effect, thermodiffusive thermopower (S_{td}), i.e., the entropy transferred by thermodiffusive ions, can be defined as the ratio between the build-in electric field $-dV/dx$ and the temperature gradient dT/dx:

$$S_{td} = -\frac{dV/dx}{dT/dx} = -\frac{V(T_H) - V(T_C)}{T_H - T_C} \quad (1)$$

where V is the voltage, T_H and T_C are the temperatures at the hot electrode and the cold electrode, respectively. Hence, for a p-type thermodiffusive thermopower ($S_{td} > 0$), the voltage is negative if the positive electrode is attached to the hot electrode. There is an internal electric field pointing from T_C to T_H, which is induced by a larger cation diffusion coefficient compared to anion, i.e., cation moving faster.

For the thermogalvanic effect, thermopower arises from the nonequilibrium redox reactions at the hot electrode and the cold electrode, which is a manifestation of the temperature-dependent standard electrode potential (E^0) of redox couples. In an electrochemistry system, the temperature dependence of E^0 is indeed referred to as the temperature coefficient (α_R), which can be measured based on the change of E^0 with respect to temperature rise in an isothermal half-cell:

$$\alpha_R = \frac{dE^0}{dT} \tag{2}$$

Similar to the thermoelectric,[S2] thermopower only from thermogalvanic effect (S_{tg}) can be written as following equation[S3]:

$$S_{tg} = -\frac{E^0(T_H) - E^0(T_C)}{T_H - T_C} = -\alpha_R \tag{3}$$

Eq (3) simply indicates that a p-type S_{tg} (> 0) has a negative temperature coefficient of the standard electrode potential, where the voltage is negative if the positive electrode is attached to the hot electrode.

In the ionic gels system, the voltage from the thermodiffusion effect is not negligible, because the strong interaction between charged organic substrate and mobile ions causes a large concentration profile from the different diffusion coefficients between cations and anions. Hence, the measured ionic thermopower (S_i) for gels G-*m/n* $FeCN^{4-/3-}$ and G-*x/y* I^-/I_3^- is a total value of thermogalvanic effect (S_{tg}) and thermodiffusion effect (S_{td}), which the corresponding ionic thermopower is shown in Fig. S2-S3. It is noted that in gels G-*x/y* I^-/I_3^-, total thermopower is p-type while the thermogalvanic effect exhibits n-type (i.e., $\alpha_R > 0$). S_{td} from the thermodiffusion effect dominates the total ionic thermopower because of the lower value of $S_{tg}(I^-/I_3^-)$ (Fig. S3-S4).

Note 3. Selection of built-in electrodes between asymmetric gels

In the construction of i-TE-EC cells, three kinds of materials, i.e., graphite paper, platinum foil, and Celgard 2400 membrane, are chosen as built-in electrodes. The potential difference ($\Delta\Phi$) shows that only graphite paper can generate a maximum $\Delta\Phi$ between the asymmetric gels (Fig. S7). As known to all, ions cannot flow across the platinum metal, which forbids the ions conductivity. And electrolyte can't penetrate into an organic Celgard 2400 membrane with bad wettability, as well as electrical insulator resulting in an open circuit inside the i-TE-EC cell. From the characteristics of three types of electrodes, two factors are required for the accessible electrodes. (a) ion permeability. It allows ion penetration to achieve conductivity, supporting ions

exchange between two separate electrolytes for balancing internal charge. (b) hydrophilia. The hydrophilic membrane can ensure the adequate contact with electrolyte and the transfer of ion. Moreover, for maintaining the $\Delta\Phi$, the built-in electrodes should have the ability to control the diffusion of redox ions (e.g., $FeCN^{4-/3-}$ and I^-/I_3^-).

In addition, we use another Nafion™ perfluorosulfonic acid cation exchange membrane (CEM) (DuPont Co. Ltd) as the built-in electrode as a comparison with graphite paper. An i-TE-EC cell with the optimized gel composition using CEM shows a higher $\Delta\Phi$ at the same temperature and hence an improved performance including higher output power and energy density (Fig. S21), compared with the i-TE-EC cell using graphite paper. Moreover, the i-TE-EC cell using CEM has a longer life span than graphite paper, due to the stronger ability to prevent the diffusion of redox ions. However, in a real application, material costs should be considered as an important factor. Graphite paper has the low cost advantage, e.g., a 250×200 mm only costs about ¥20, while a CEM membrane purchased from DuPont Co., Ltd. costs more, e.g., an N117 100×100 mm costs about ¥350. Therefore, considering this point, only graphite paper is used as the built-in electrode throughout the work unless otherwise stated.

Note 4. Carnot-relative efficiency calculation

Heat-to-electricity conversion ability of i-TE-EC cells can be evaluated by Carnot-relative efficiency, calculated according to following Eq (4). [S3]

$$\eta_r = \frac{\eta}{\eta_{Carnot}} = \frac{\tau_{dis}}{\tau_{ch} + \tau_{dis}} \frac{P_{ave}}{(\Delta T)^2} T_H \frac{d}{\lambda} \quad (4)$$

where d, λ, P_{ave}, and T_H represent the area and thickness of the i-TE-EC cell, thermal conductivity, average power density during the discharge time, and high-side temperature, respectively. τ_{dis} is the electrical discharge time and τ_{ch} is the thermal charge time. Thermal conductivity λ is calculated according to the relationship of $\lambda = \rho D C_p$, where thermal diffusive coefficient D and specific heat capacity C_p are simultaneously obtained by the laser flash method (LAF 467; Netzsch), and bulk density ρ is obtained by Archimedean method. As a result, λ of composited gels G-

0.175/0.025 M $FeCN^{4-/3-}$ and G-0.10/0.05 M I^-/I_3^--0.4 M CF_3SO_3K is obtained according to the measured data, showing gradually increased values of 0.05, 0.06, 0.08, 0.11, and 0.15 W m^{-1} K^{-1} at 293, 298, 303, 308, and 313 K, respectively (Fig. S37).

Optimized i-TE-EC cell Gp | G-0.175/0.025 M $FeCN^{4-/3-}$ | Gp | G-0.10/0.05 M I^-/I_3^--0.4 M CF_3SO_3K | Gp is used for Carnot-relative efficiency calculation. Power vs. time is obtained in the thermal discharge at R = 5 kΩ and T_C = 313 K (ΔT = 5 K) (Fig. 4(g)). Required parameters for calculation are obtained: T_H = 318 K, ΔT = 5 K, τ_{ch} = 1260 s, τ_{dis} = 7200 s, calculated P_{ave} = 0.012 W m^{-2} (2 h discharge), λ = 0.15 W m^{-1} K^{-1} (experimentally measured), and d = 4 mm. Efficiency η_r is calculated by substituting above parameters into Eq (4).

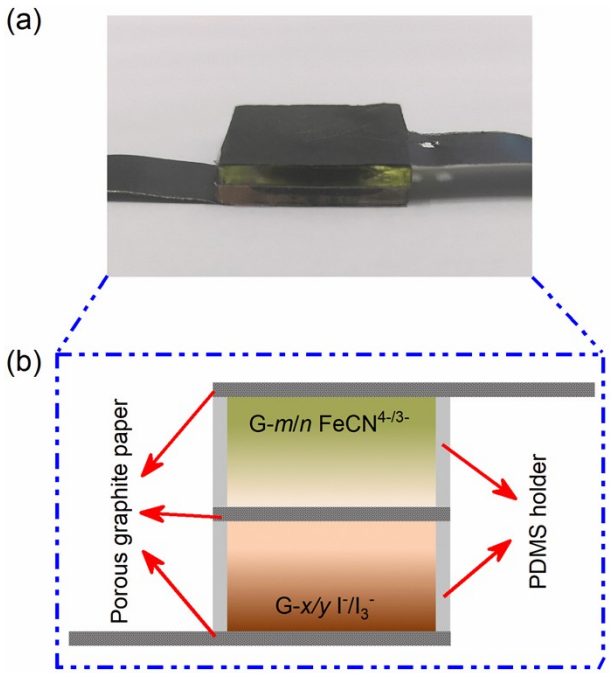

Fig. S1. (a) Real image of fabricated i-TE-EC cell; (b) Constituent of i-TE-EC cell with asymmetric gels G-*m*/*n* $FeCN^{4-/3-}$ and G-*x*/*y* I^-/I_3^-.

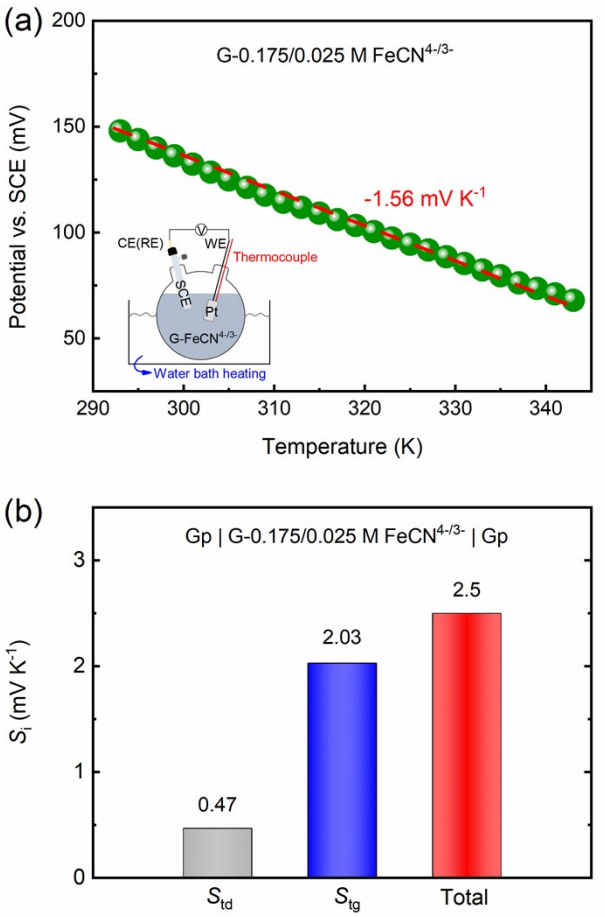

Fig. S2. (a) Electrode potential vs. SCE as a function of temperature (293~343 K) for gels G-0.175/0.025 M $FeCN^{4-/3-}$ using Pt as a working electrode and SCE as counter and reference electrodes. Inset: the test schematic; (b) Ionic thermopower (S_i) from thermodiffusion effect (S_{td}) and thermogalvanic effect (S_{tg}), and total S_i for i-TE cell Gp | G-0.175/0.025 M $FeCN^{4-/3-}$ | Gp at 293 K.

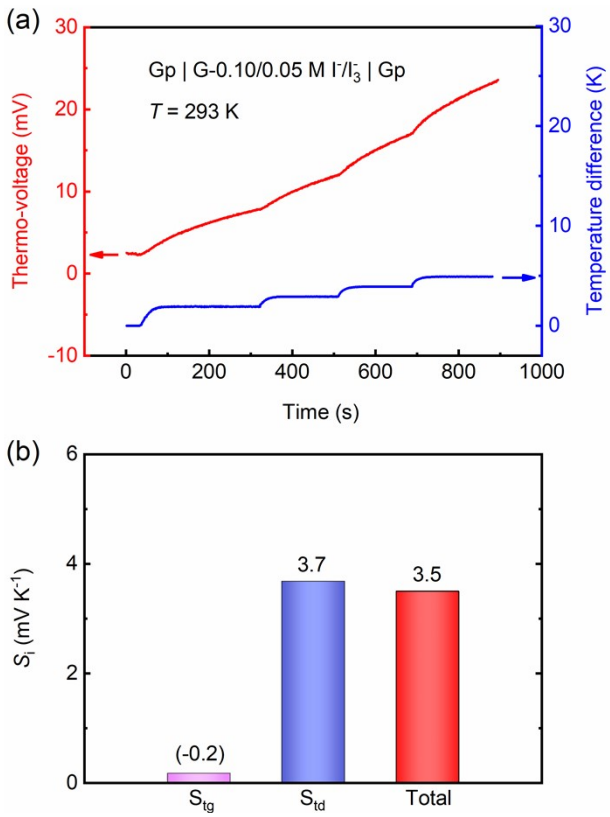

Fig. S3. (a) Thermo-voltage and temperature differences with dependent on time (ΔT = 2, 3, 4, 5 K); (b) Corresponding ionic thermopower (S_i) from thermogalvanic effect (S_{tg}), thermodiffusion effect (S_{td}), and total S_i for i-TE cell Gp | G-0.10/0.05 M I^-/I_3^- | Gp at 293 K.

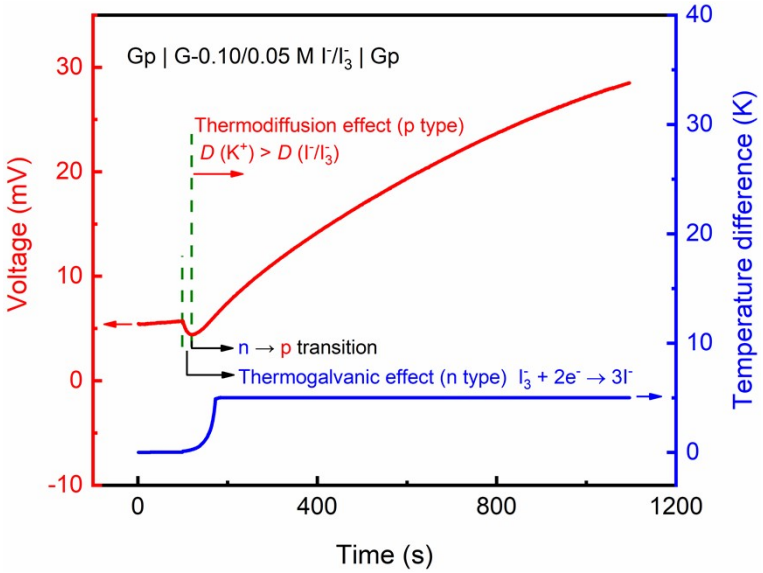

Fig. S4. Voltage and temperature difference (ΔT) with dependent of time for i-TE cell Gp | G-0.10/0.05 M I^-/I_3^- | Gp. The initial decline in voltage suggests a thermogalvanic effect (n-type) from redox reaction $I_3^- + 2e^- \rightleftharpoons I^-$, and then an increase in voltage suggests a thermodiffusion effect (p-type, predominant result), due to the ion concentration difference from different ion diffusion coefficients ($v(K^+) > v(I^-/I_3^-)$) when applying ΔT.

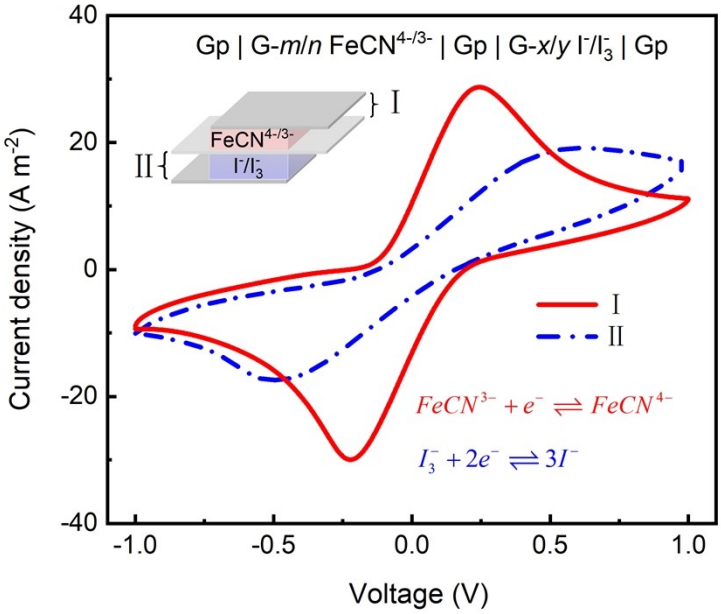

Fig. S5. Cyclic voltammetry (CV) curves of two parts (I and II) in i-TE-EC cells Gp | G-*m*/*n* $FeCN^{4-/3-}$ | Gp | G-*x*/*y* I^-/I_3^- | Gp. The peaks at ±0.24 V and ±0.5 V correspond to the redox reaction of $FeCN^{3-} + e^- \rightleftharpoons FeCN^{4-}$ and $I_3^- + 2e^- \rightleftharpoons 3I^-$, respectively.

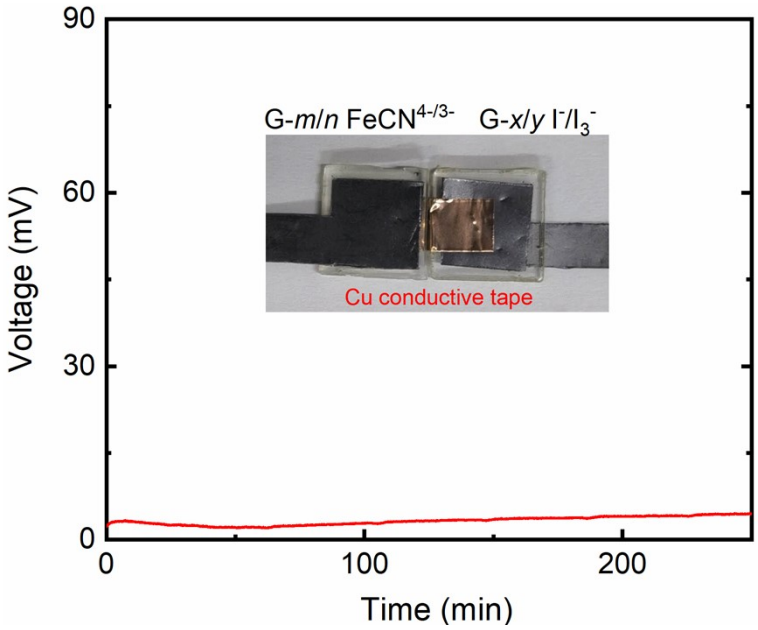

Fig. S6. The i-TE cell is Gp | G-*m*/*n* $FeCN^{4-/3-}$ | Gp and Gp | G-*x*/*y* I^-/I_3^- | Gp, which is connected by a copper conductive gap.

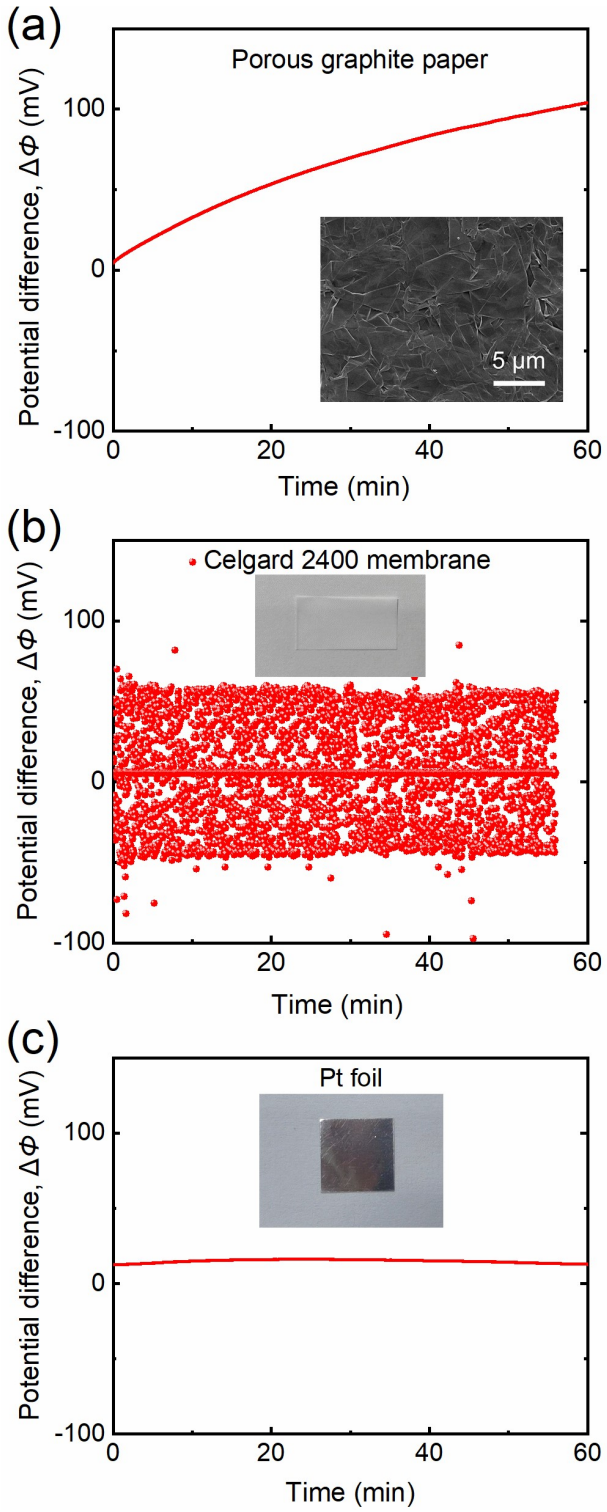

Fig. S7. Potential difference ($\Delta\Phi$) as a function of time for i-TE-EC cells with three types of built-in electrodes. (a) Porous graphite paper (Gp); (b) Celgard 2400 membrane; (c) Pt foil. Inset: SEM image of Gp, and real image of Celgard 2400 and Pt foil, respectively.

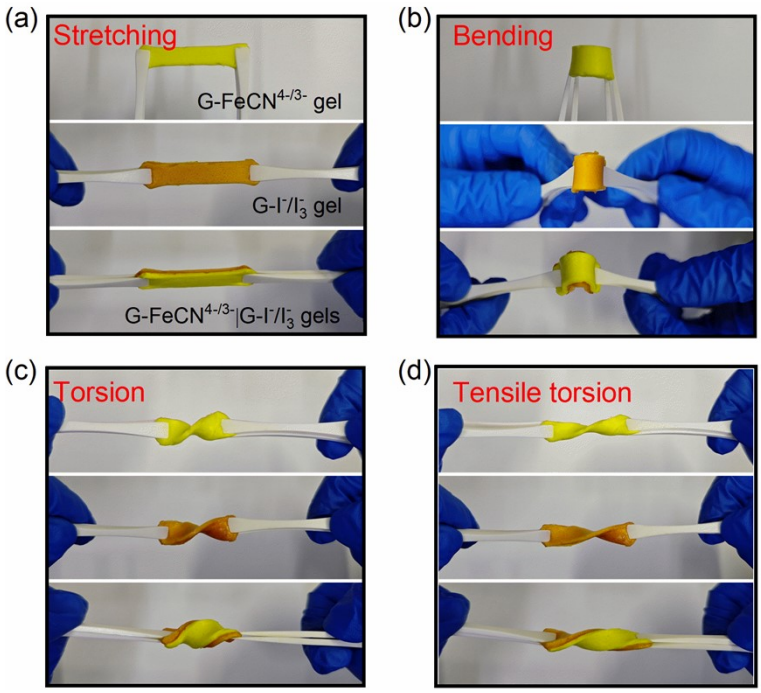

Fig. S8. Mechanical properties for gels G-*m*/*n* $FeCN^{4-/3-}$, G-*x*/*y* I^-/I_3^-, and G-*m*/*n* $FeCN^{4-/3-}$|G-*x*/*y* I^-/I_3^-. (a) Stretching, (b) Bending, (c) Torsion, and (d) Tensile torsion.

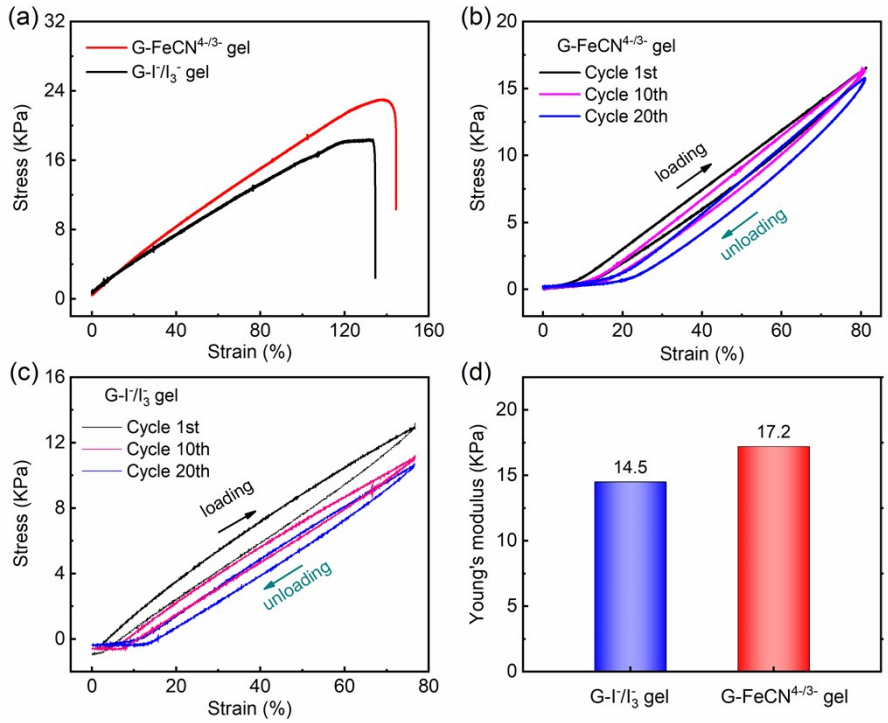

Fig. S9. Mechanical properties of gels G-$FeCN^{4-/3-}$ and G-I^-/I_3^-. (a) Strain-stress curves; (b) Strain-stress curves for gels G-0.175/0.025 M $FeCN^{4-/3-}$ (b) and G-0.10/0.05 M I^-/I_3^- (c) at the 1st, 10th and 20th cycles under loading-unloading operations; (d) Young's modulus of gels obtained from strain-stress curves.

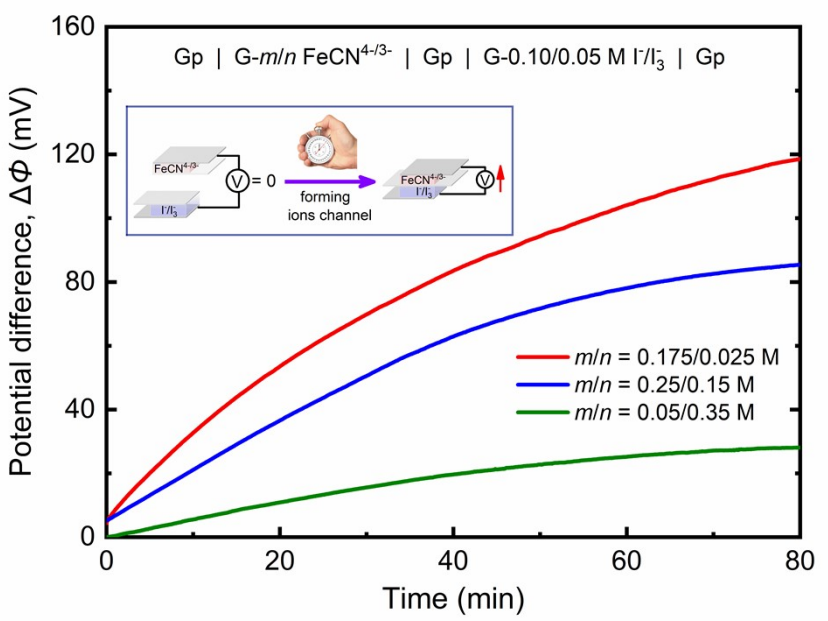

Fig. S10. The i-TE-EC cell is Gp | G-*m*/*n* $FeCN^{4-/3-}$ | Gp | G-0.10/0.05 M I^-/I_3^- | Gp (*m*/*n* = 0.05/0.35, 0.25/0.15, and 0.175/0.025 M). Inset: gradually established ions channel after assembling i-TE-EC cell from single cell Gp | G-*m*/*n* $FeCN^{4-/3-}$ | Gp and Gp | G-0.10/0.05 M I^-/I_3^- | Gp. $\Delta\Phi$ is near zero when initially fabricating i-TE-EC cell, and increases as increasing times due to the ions diffusing through the built-in Gp. Different *m*/*n* values result in different $\Delta\Phi$ after 80 min.

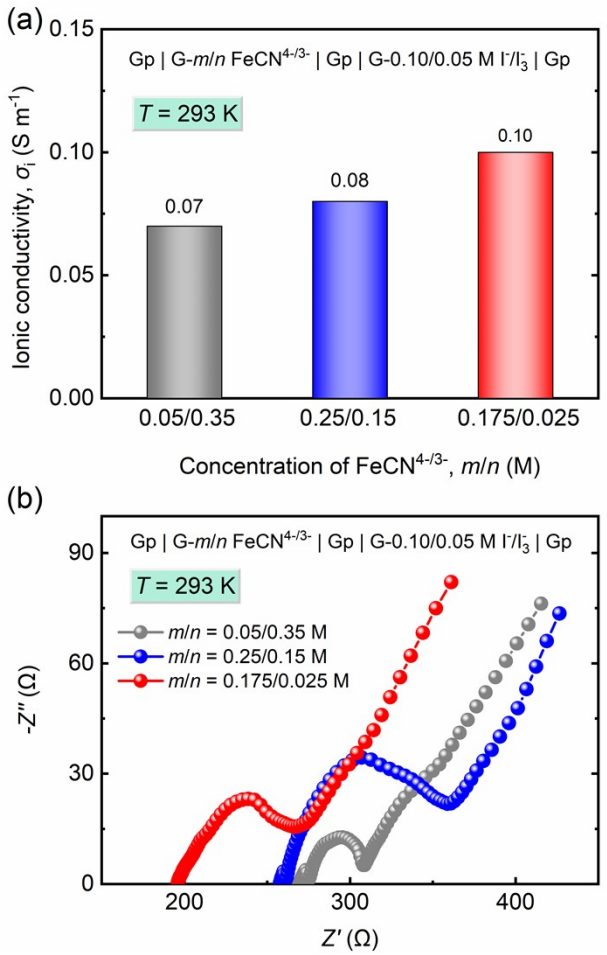

Fig. S11. (a) Ionic conductivity (σ_i) and (b) Nyquist plots of electrochemical impedance spectroscopy (EIS) for i-TE-EC cell Gp | G-*m*/*n* $FeCN^{4-/3-}$ | Gp | G-0.10/0.05 M I^-/I_3^- | Gp (*m*/*n* = 0.05/0.35, 0.25/0.15 and 0.175/0.025 M) at 293 K.

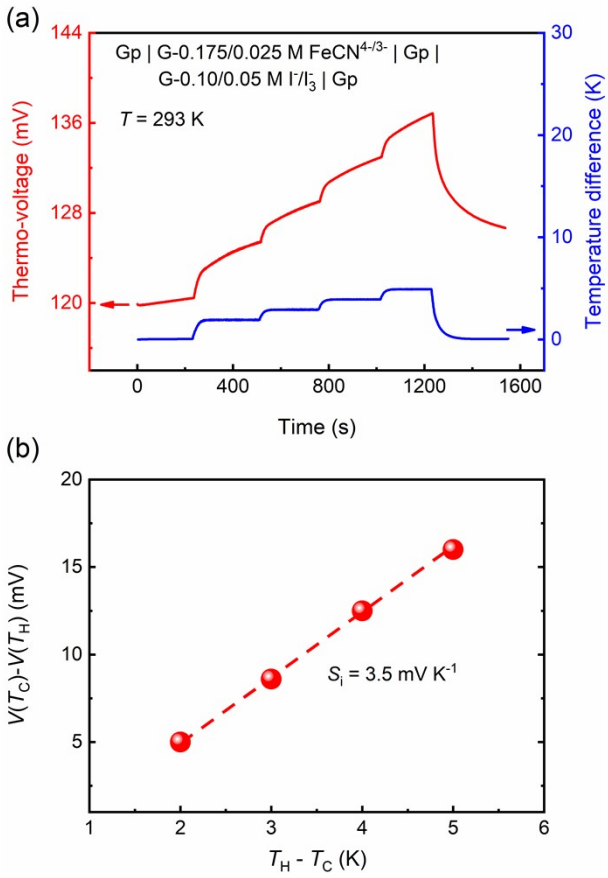

Fig. S12. (a) Thermo-voltage and temperature difference vs. time (ΔT = 2, 3, 4, 5 K); (b) $V(T_C)$ - $V(T_H)$ vs. T_H - T_C for i-TE-EC cell Gp | G-0.175/0.025 M $FeCN^{4-/3-}$ | Gp | G-0.10/0.05 M I^-/I_3^- | Gp at T = 293 K.

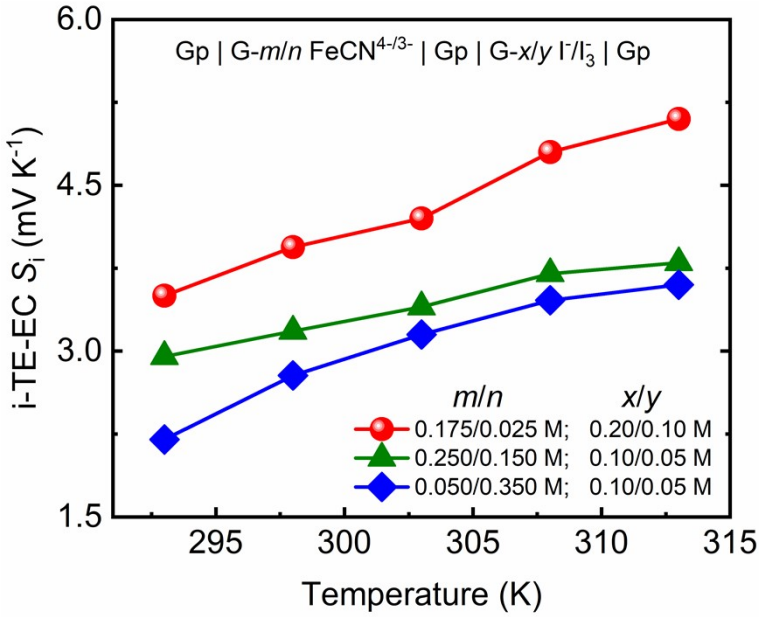

Fig. S13. The i-TE-EC cell S_i for Gp | G-m/n M $FeCN^{4-/3-}$ | Gp | G-x/y M I^-/I_3^- | Gp (m/n = 0.25/0.15 and 0.05/0.35 M for x/y = 0.10/0.05 M; m/n = 0.175/0.025 M, x/y = 0.2/0.1 M) at 293-313 K.

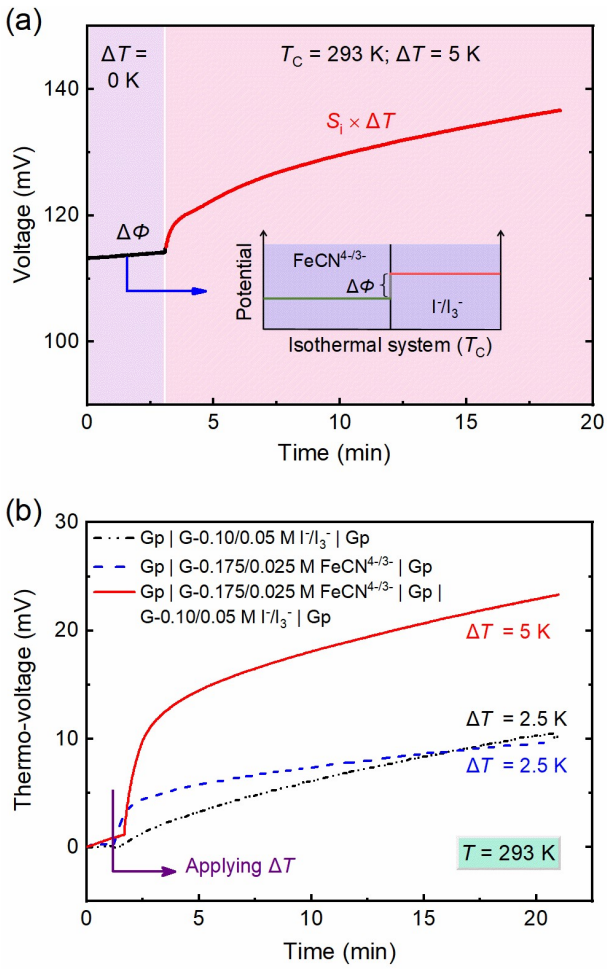

Fig. S14. (a) Voltage as a function of time for i-TE-EC cell Gp | G-0.175/0.025 M $FeCN^{4-/3-}$ | Gp | G-0.10/0.05 M I^-/I_3^- | Gp at T_C = 293 K and ΔT = 5 K, inset shows potential distributions inside i-TE-EC under the isothermal system; (b) Thermo-voltage as a function of time for i-TE-EC cell Gp | G-0.175/0.025 M $FeCN^{4-/3-}$ | Gp | G-0.10/0.05 M I^-/I_3^- | Gp, and single cell Gp | G-0.175/0.025 M $FeCN^{4-/3-}$ | Gp and Gp | G-0.10/0.05 M I^-/I_3^- | Gp at ΔT = 5 and 2.5 K.

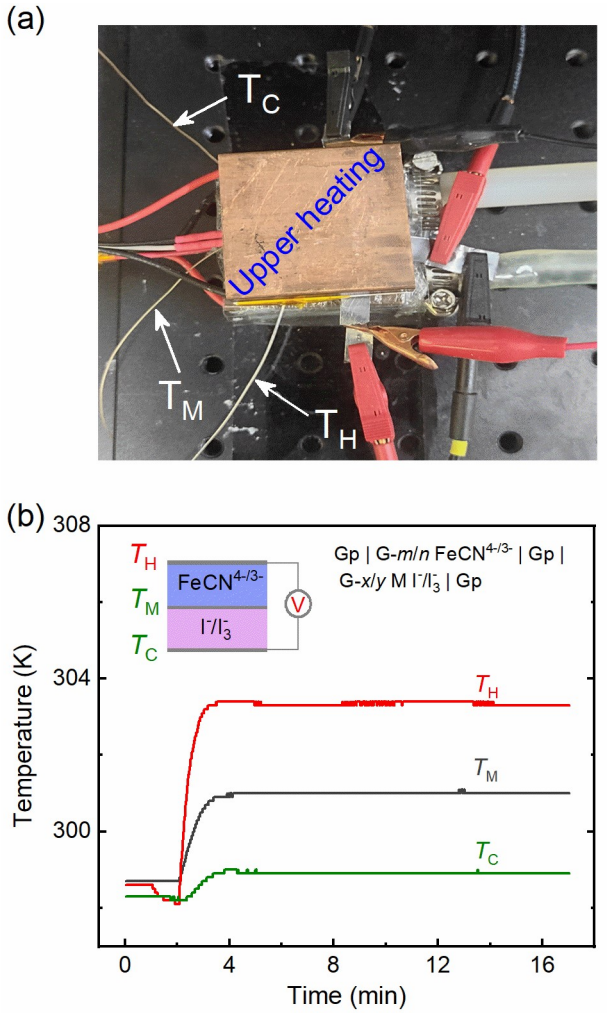

Fig. S15. (a) Practical test graph; (b) Temperature variation at the hot side (T_H), middle (T_M), and cold side (T_C) with time for i-TE-EC cell Gp | G-*m*/*n* $FeCN^{4-/3-}$ | Gp | G-*x*/*y* I^-/I_3^- | Gp at 298 K and ΔT = 5 K. Inset: an equivalent heat transfer. The corresponding T_H, T_M, and T_C increased as subjecting temperature difference ΔT between the top and bottom electrodes. In such i-TE-EC cell, T_M was the middle value of T_H and T_C, i.e., $T_H = (T_M + T_C)/2$.

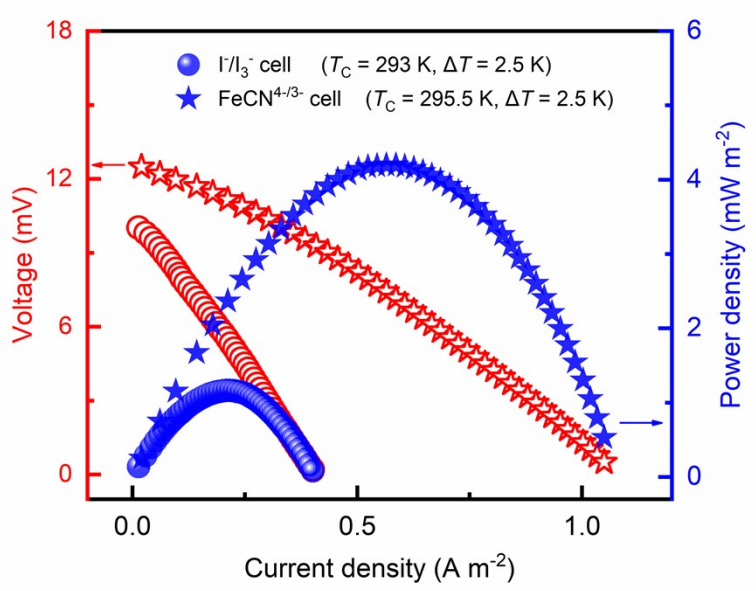

Fig. S16. Voltage-current density-power density curves for single cells Gp | G-0.175/0.025 M $FeCN^{4-/3-}$ | Gp and Gp | G-0.10/0.05 M I^-/I_3^- | Gp at corresponding temperature (T_C) and temperature difference (ΔT).

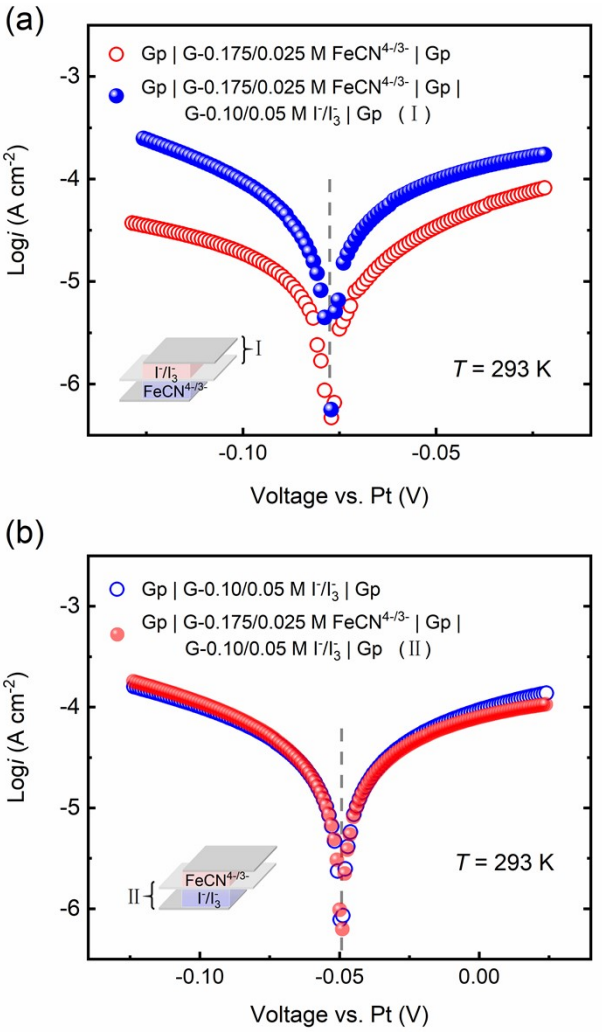

Fig. S17. Comparison of Tafel curves between i-TE-EC cell and single cells. (a) Part (I) in i-TE-EC cell Gp | G-0.175/0.025 M $FeCN^{4-/3-}$ | Gp | G-0.10/0.05 M I^-/I_3^- | Gp and single cell Gp | G-0.175/0.025 M $FeCN^{4-/3-}$ | Gp; (b) Part (II) in i-TE-EC cell Gp | G-0.175/0.025 M $FeCN^{4-/3-}$ | Gp | G-0.10/0.05 M I^-/I_3^- | Gp and single cell Gp | G-0.10/0.05 M I^-/I_3^- | Gp.

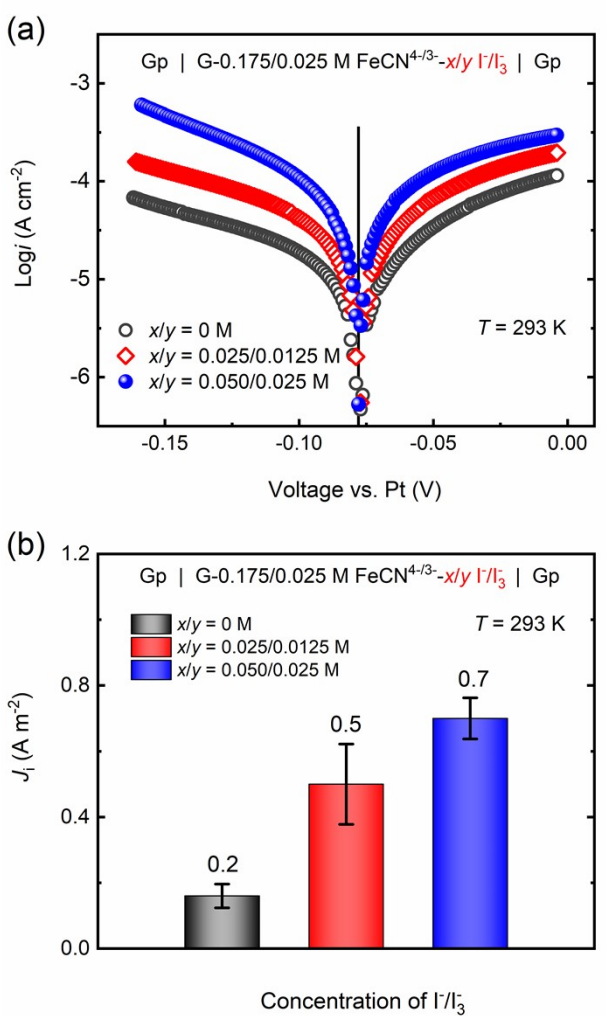

Fig. S18. (a) Tafel curves and (b) exchange current density (J_i) for i-TE-EC cell Gp | G-0.175/0.025 M $FeCN^{4-/3-}$-*x*/*y* I^-/I_3^- | Gp (*x*/*y* = 0, 0.025/0.0125 and 0.050/0.025 M) at 293 K.

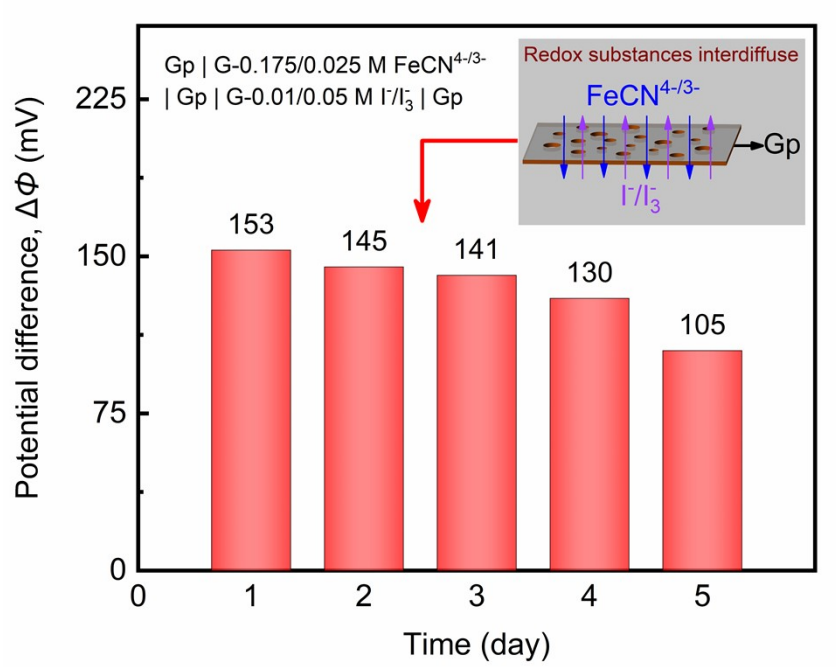

Fig. S19. Potential difference decay of i-TE-EC cell Gp | G-0.175/0.025 M $FeCN^{4-/3-}$ | Gp | G-0.10/0.05 M I^-/I_3^- | Gp for 5 consecutive days. Inset: the interdiffusion of two types of redox couples.

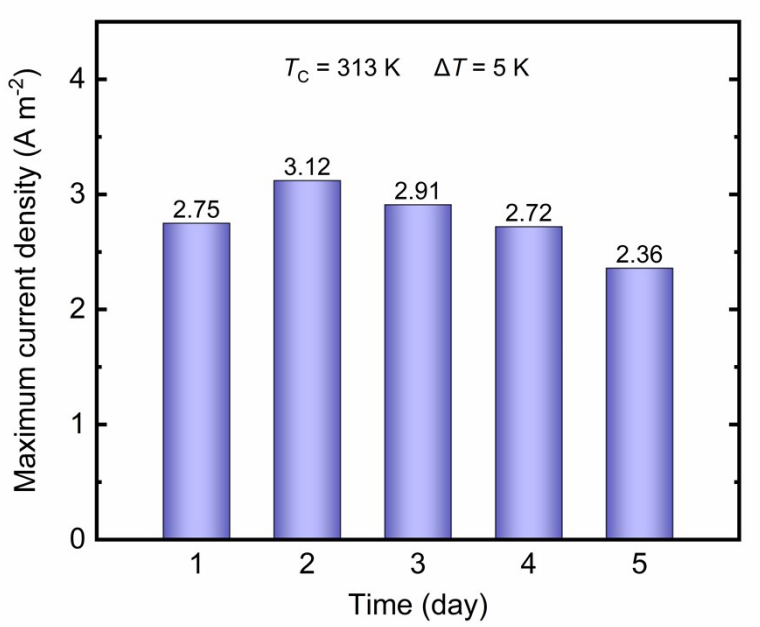

Fig. S20. Variation of maximum current density. It is calculated from the *I-V* discharge process for i-TE-EC cell Gp | G-0.175/0.025 M $FeCN^{4-/3-}$ | Gp | G-0.10/0.05 M I^-/I_3^- | Gp in 5 consecutive days (T_C = 313 K, ΔT = 5 K).

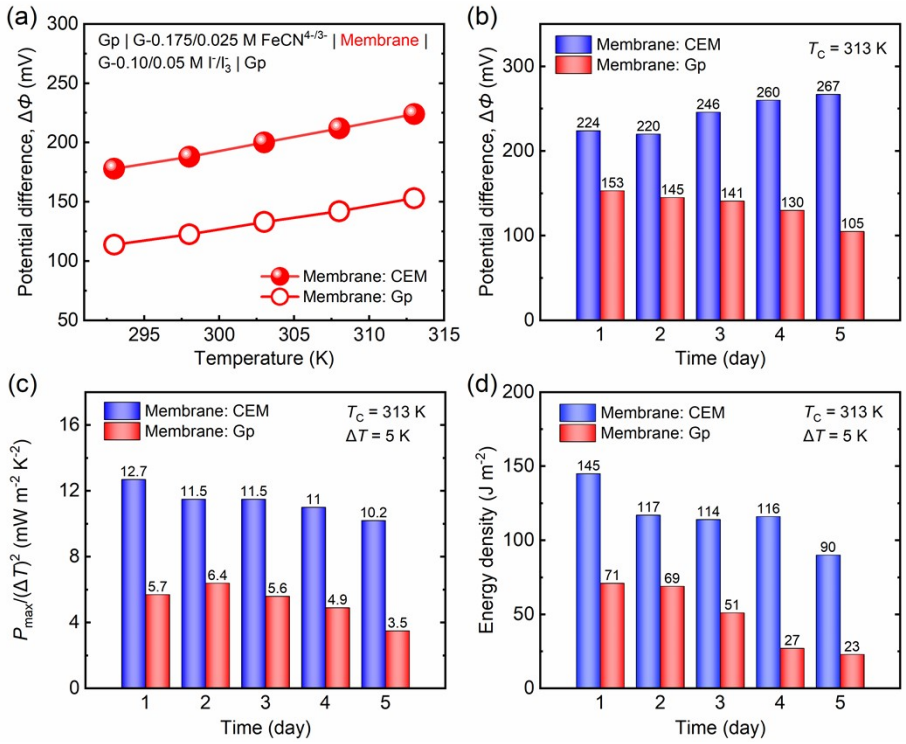

Fig. S21. Comparison of potential difference ($\Delta\Phi$) and life-span performance for i-TE-EC cell Gp | G-m/n $FeCN^{4-/3-}$ | membrane | G-x/y I^-/I_3^- | Gp (m/n = 0.175/0.025 M; x/y = 0.10/0.05 M). (a) $\Delta\Phi$ with dependence of temperature. (b) $\Delta\Phi$, (c) $P_{max}/(\Delta T)^{2,}$ and (d) energy density at T_C = 313 K for 5 days. Membrane: CEM and Gp. The external resistor of 7.5 kΩ for harvesting energy; ΔT = 5 K.

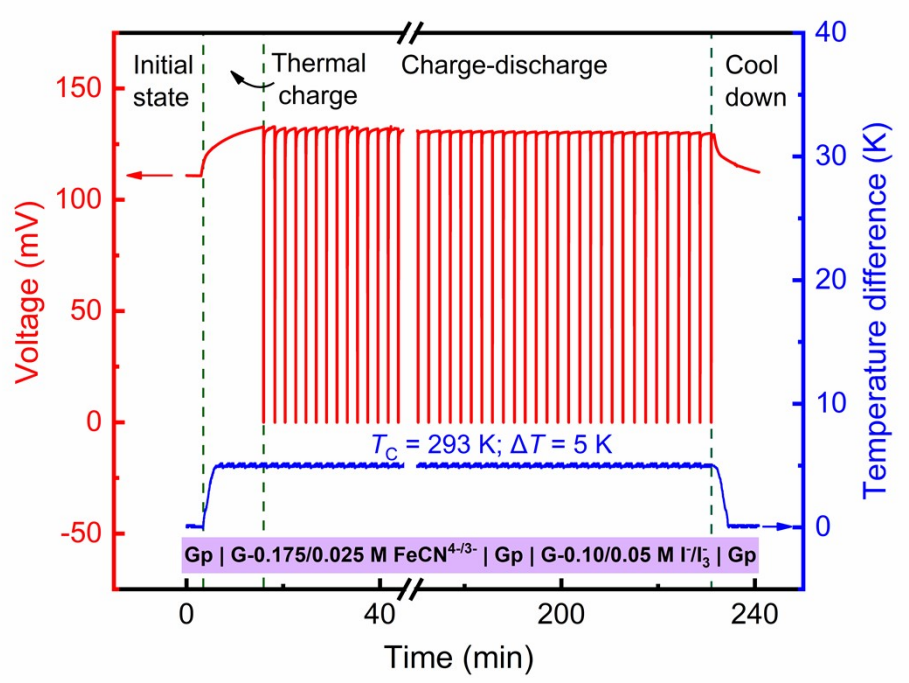

Fig. S22. Quasi-continuous discharge of voltage and temperature difference with dependence of time. The quasi-continuous discharge includes the initial state, thermal charge, charge-discharge, and cool-down process at T_C = 293 K and ΔT = 5 K. The i-TE-EC cell is Gp | G-0.175/0.025 M $FeCN^{4-/3-}$ | Gp | G-0.10/0.05 M I^-/I_3^- | Gp.

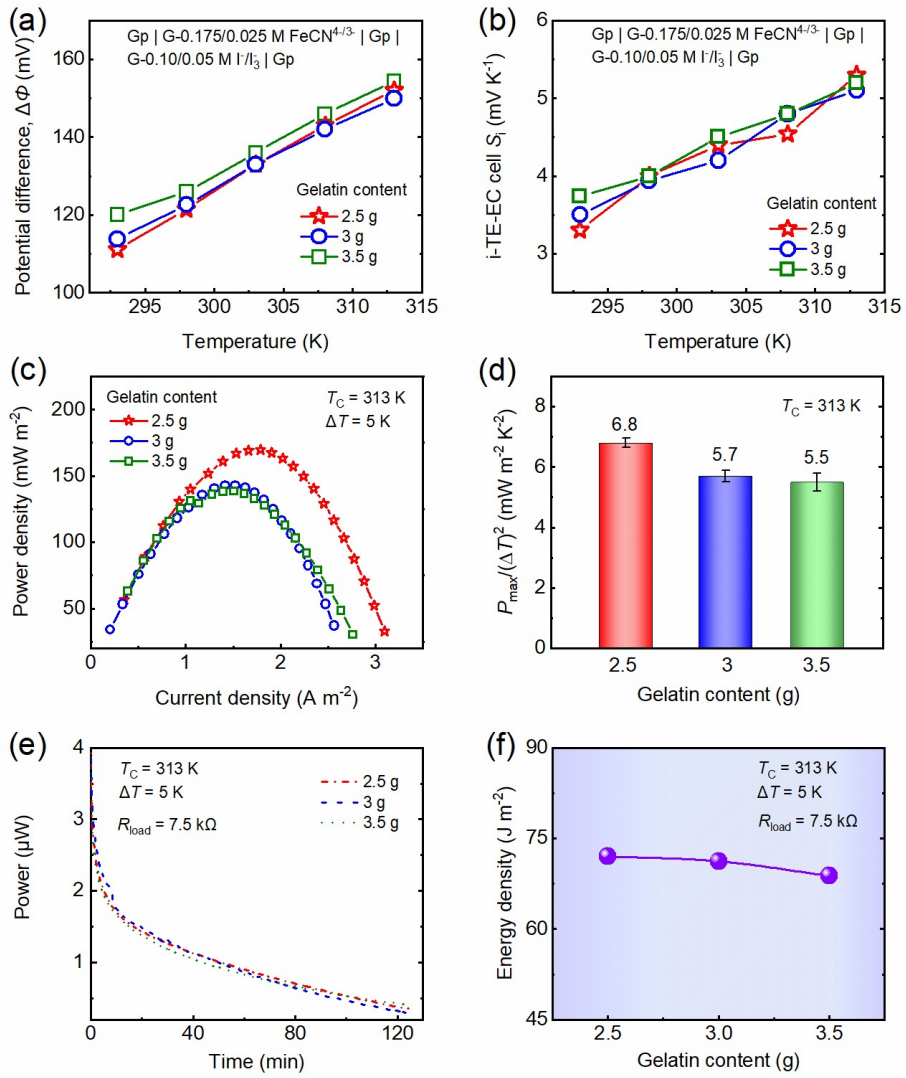

Fig. S23. Effect of gelatin content on performance of i-TE-EC cell Gp | G-0.175/0.025 M $FeCN^{4-/3-}$ | Gp | G-0.10/0.05 M I^-/I_3^- | Gp. (a) Potential difference as a function of temperature. (b) i-TE-EC cell S_i vs. temperature. (c) Power density-current density curves at T_C = 313 and ΔT = 5 K. (d) $P_{max}/(\Delta T)^2$ vs. gelatin content at T_C = 313 and ΔT = 5 K. (e) Power with the dependence of time at T_C = 313 and ΔT = 5 K. (f) Energy density vs. gelatin content at same external resistances R_{load} = 7.5 kΩ. A total volume of 8 ml water is used.

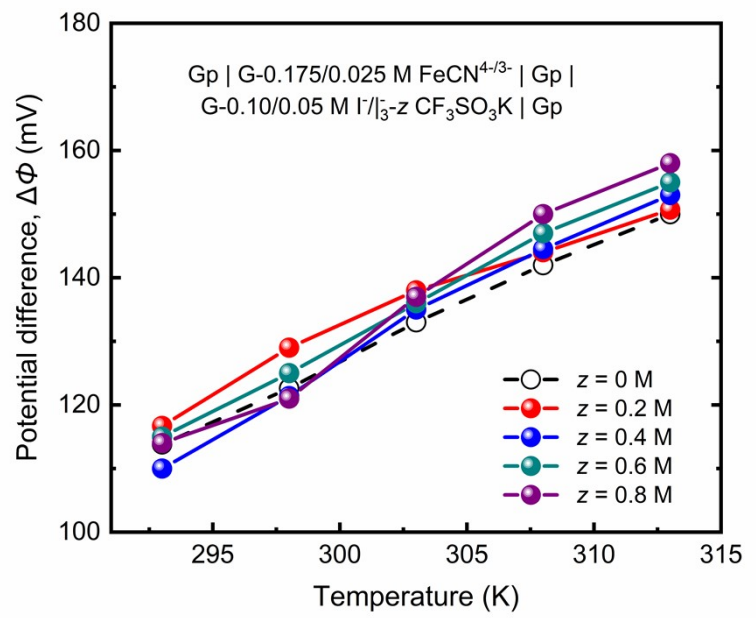

Fig. S24. Potential difference at different temperatures. The i-TE-EC cell is Gp | G-0.175/0.025 M $FeCN^{4-/3-}$ | Gp | G-0.10/0.05 M I^-/I_3^--*z* CF_3SO_3K | Gp (*z* = 0, 0.2, 0.4, 0.6, and 0.8 M).

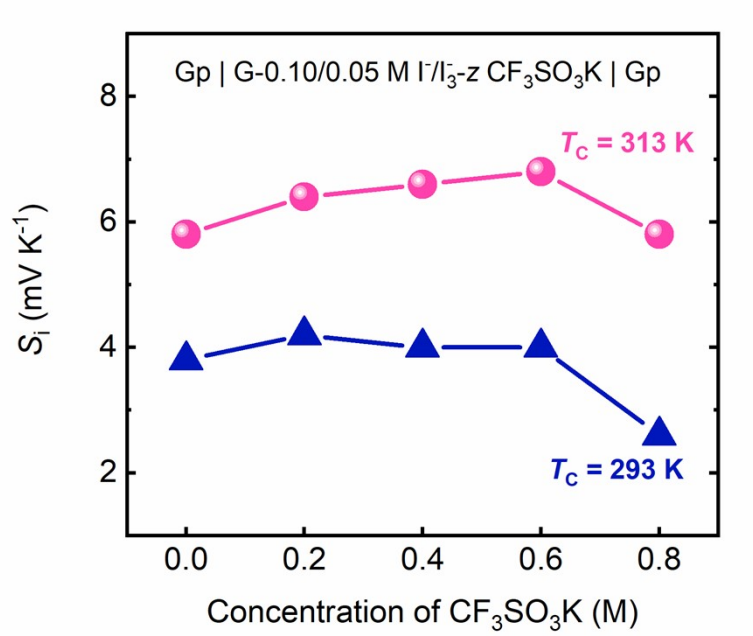

Fig. S25. Ionic thermopower (S_i) with a dependence of concentration of CF_3SO_3K at T_C = 293 K and 313 K. The i-TE cell Gp | G-0.10/0.05 M I^-/I_3^--*z* CF_3SO_3K | Gp (*z* = 0, 0.2, 0.4, 0.6, and 0.8 M) is employed.

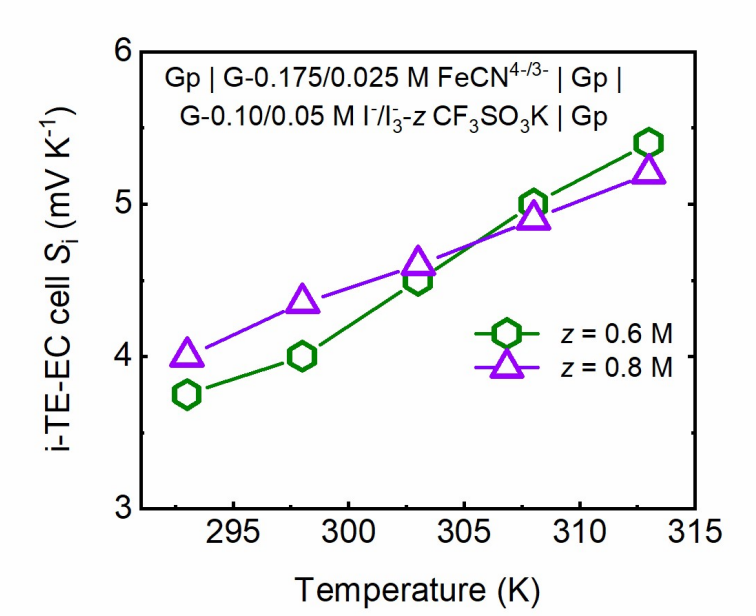

Fig. S26. Ionic thermopower S_i for i-TE-EC cells at different temperatures. The i-TE-EC cell is Gp | G-0.175/0.025 M $FeCN^{4-/3-}$ | Gp | G-0.10/0.05 M I^-/I_3^--*z* CF_3SO_3K | Gp (*z* = 0.6 and 0.8 M).

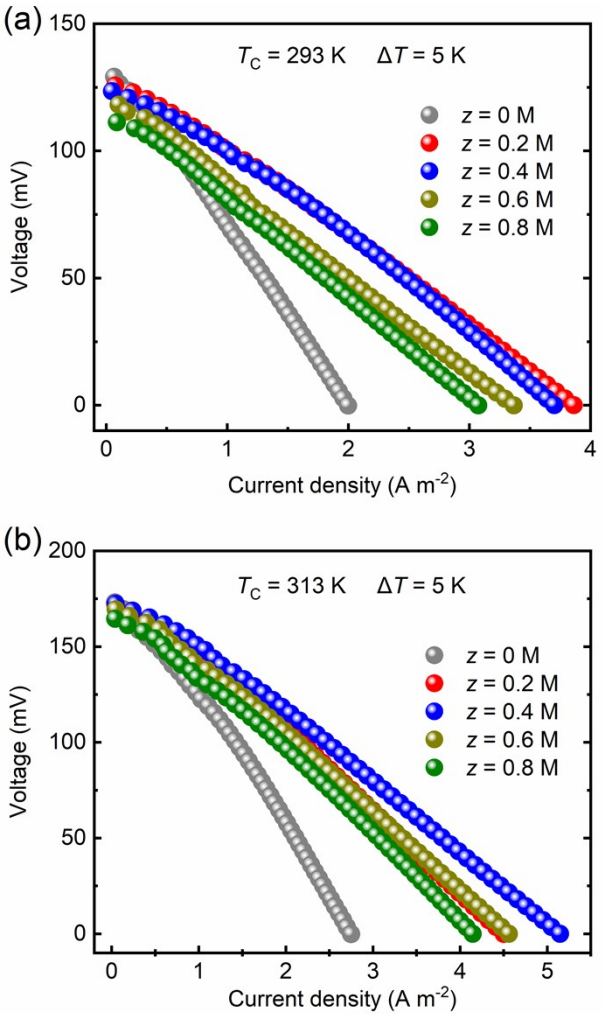

Fig. S27. Voltage-current density curves for i-TE-EC cell Gp | G-0.175/0.025 M $FeCN^{4-/3-}$ | Gp | G-0.10/0.05 M I^-/I_3^--*z* CF_3SO_3K | Gp (*z* = 0, 0.2, 0.4, 0.6 and 0.8 M). (a) T_C = 293 and ΔT = 5 K; (b) T_C = 313 K and ΔT = 5 K.

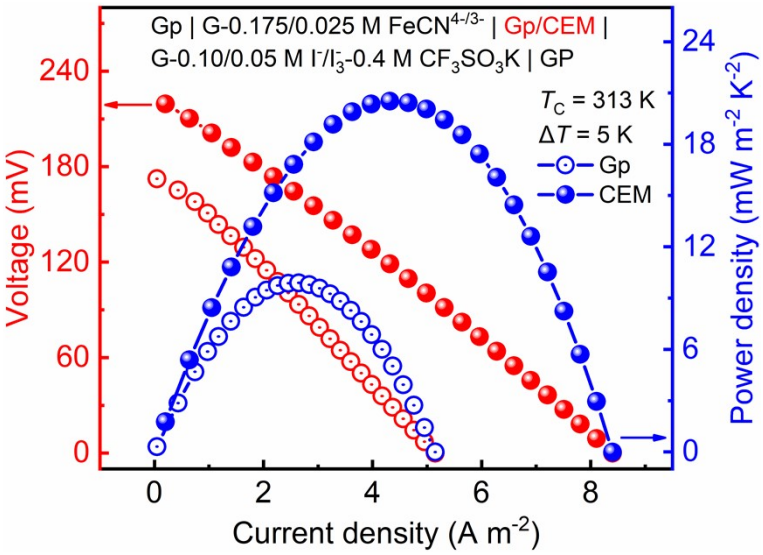

Fig. S28. Voltage-$P_{max}/(\Delta T)^2$-current density curves at T_C = 313 K and ΔT = 5 K. i-TE-EC cell: Gp | G-*m*/*n* $FeCN^{4-/3-}$ | Gp | G-*x*/*y* I^-/I_3^--*z* CF_3SO_3K | Gp; Gp | G-*m*/*n* $FeCN^{4-/3-}$ | CEM | G-*x*/*y* I^-/I_3^--*z* CF_3SO_3K | Gp. *m*/*n* = 0.175/0.025 M, *x*/*y* = 0.10/0.05 M, *z* = 0.4 M.

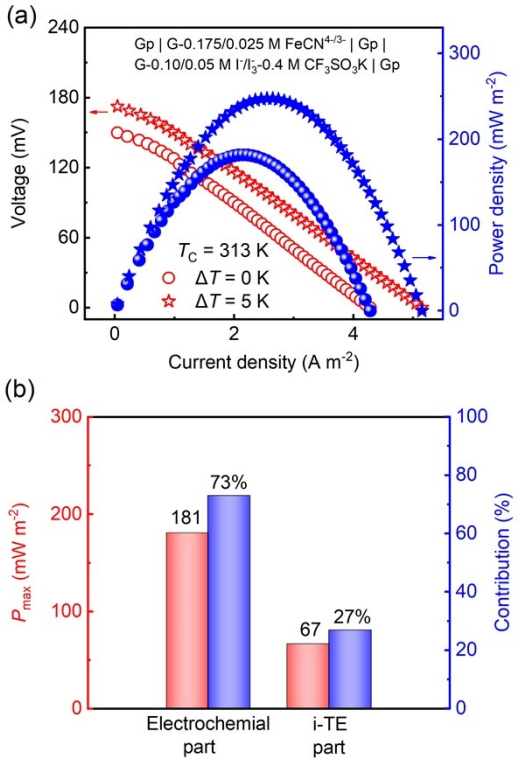

Fig. S29. Performance of i-TE-EC cell Gp | G-0.175/0.025 M $FeCN^{4-/3-}$ | Gp | G-0.10/0.05 M I^-/I_3^--0.4 M CF_3SO_3K | Gp at T_C = 313 K. (a) Voltage-power density-current density curves at T_C = 313 K with ΔT = 0 K and 5 K. (b) Power density and contribution from electrochemical part and i-TE part.

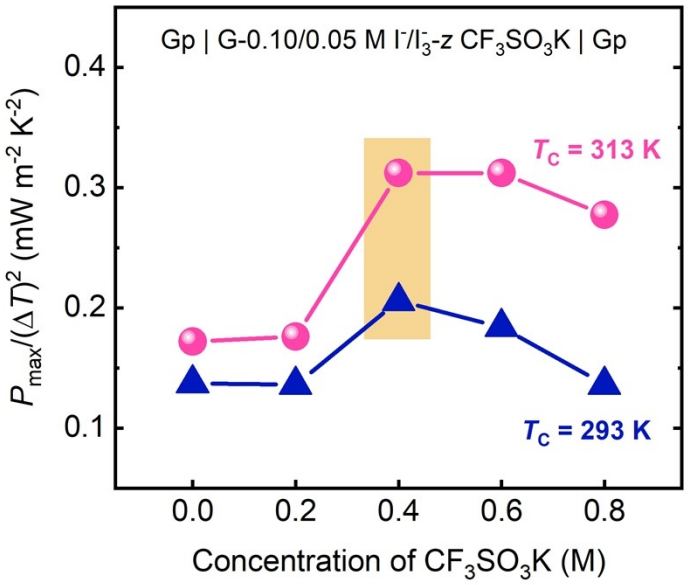

Fig. S30. Maximum output power density ($P_{max}/(\Delta T)^2$) with dependence of concentration of CF_3SO_3K at T_C = 293 K and 313 K. The i-TE cell is Gp | G-0.10/0.05 M I^-/I_3^--*z* CF_3SO_3K | Gp (*z* = 0, 0.2, 0.4, 0.6, and 0.8 M).

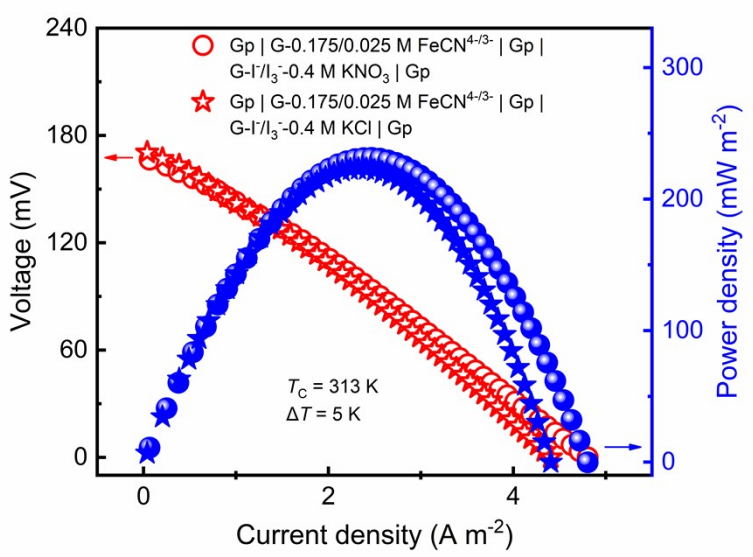

Fig. S31. Voltage-power density-current density curves. The i-TE-EC cells are Gp | G-0.175/0.025 M $FeCN^{4-/3-}$ | Gp | G-0.10/0.05 M I^-/I_3^--0.4 M KNO_3 | Gp and Gp | G-0.175/0.025 M $FeCN^{4-/3-}$ | Gp | G-0.10/0.05 M I^-/I_3^--0.4 M KCl | Gp at T_C = 313 K and ΔT = 5 K.

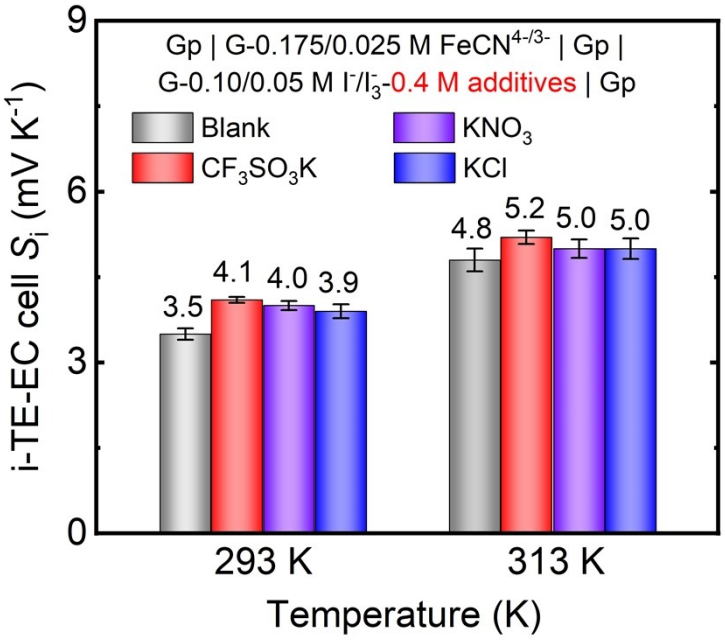

Fig. S32. The i-TE-EC cell S_i of Gp | G-0.175/0.025 M $FeCN^{4-/3-}$ | Gp | G-0.10/0.05 M I^-/I_3^--0.4 M additives | Gp at 293 and 313 K.

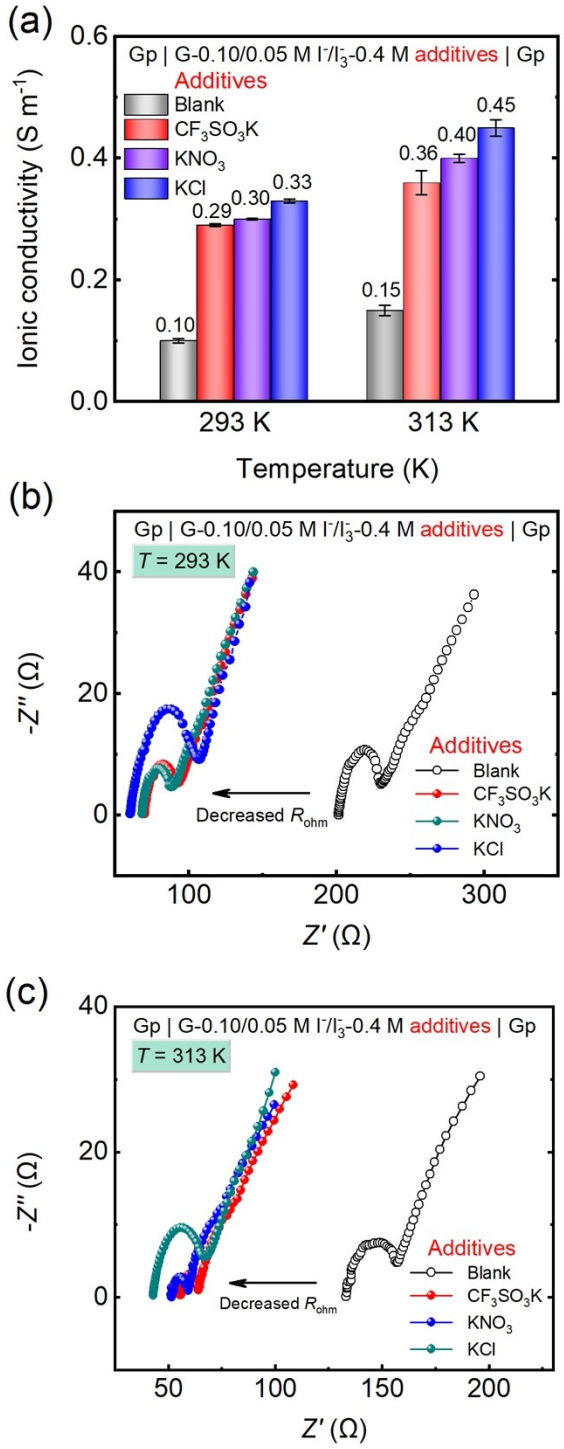

Fig. S33. Ionic conductivity of i-TE cell Gp | G-0.10/0.05 M I^-/I_3^--0.4 M additives | Gp (additives: CF_3SO_3K, KNO_3 and KCl). (a) Ionic conductivity at 293 and 313 K. Nyquist plots from EIS at 293 K (b) and 313 K (c).

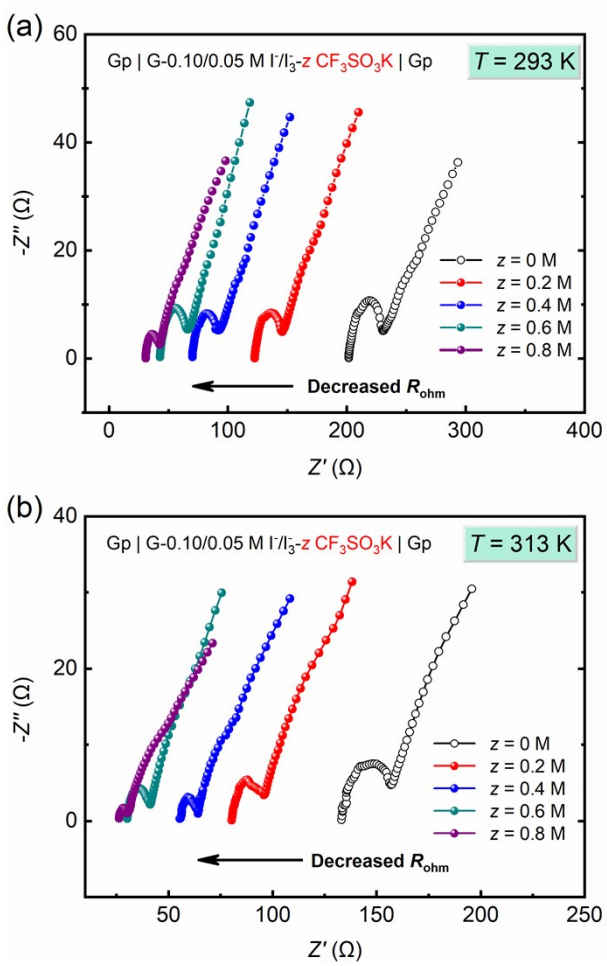

Fig. S34. Nyquist plots of i-TE cell Gp | G-0.10/0.05 M I^-/I_3^--*z* CF_3SO_3K | Gp (*z* = 0, 0.2, 0.4, 0.6, and 0.8 M). (a) 293 K and (b) 313 K.

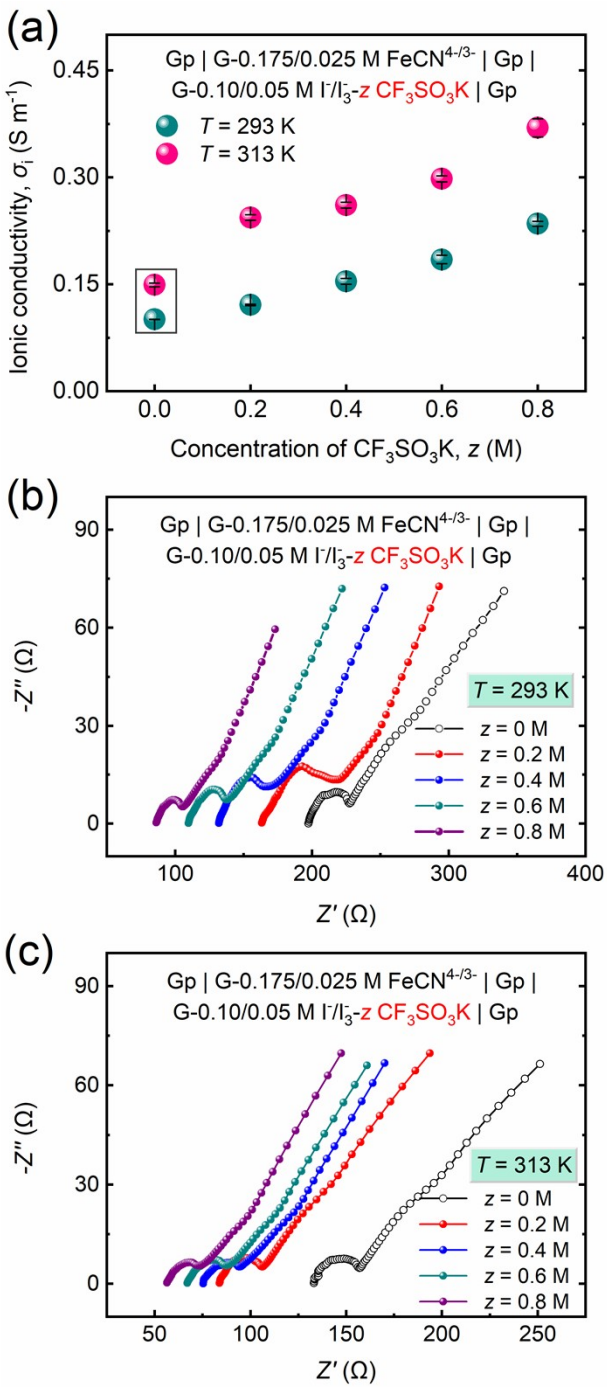

Fig. S35. (a) Ionic conductivity (σ_i) at 293 and 313 K; Nyquist plots at (b) 293 K and (c) 313 K for i-TE-EC cell Gp | G-0.175/0.025 M $FeCN^{4-/3-}$ | Gp | G-0.10/0.05 M I^-/I_3^- -*z* CF_3SO_3K | Gp (*z* = 0, 0.2, 0.4, 0.6, and 0.8 M).

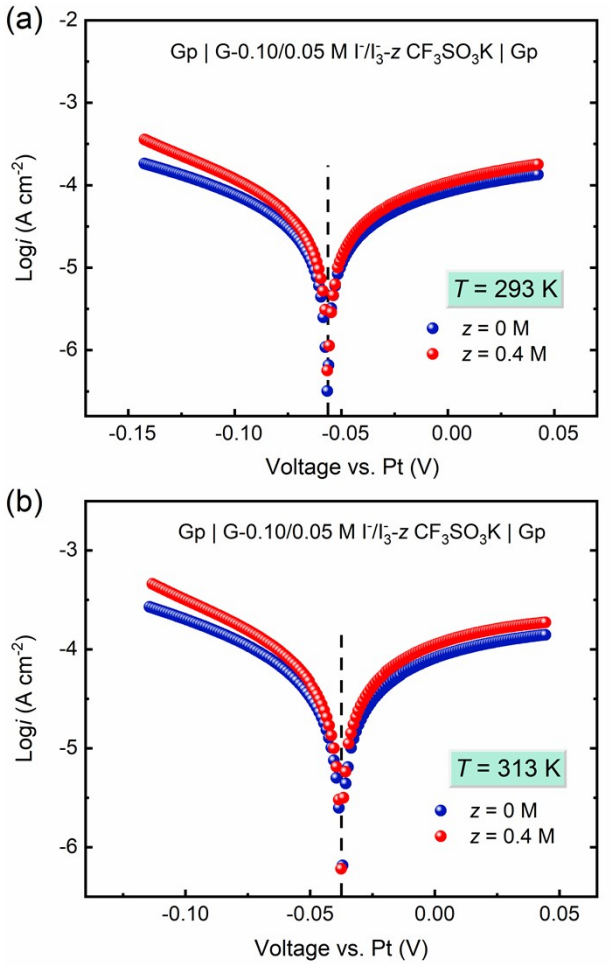

Fig. S36. Tafel curves for i-TE cell Gp | G-0.10/0.05 M I^-/I_3^--*z* CF_3SO_3K | Gp (*z* = 0 and 0.4 M). (a) 293 K and (b) 313 K.

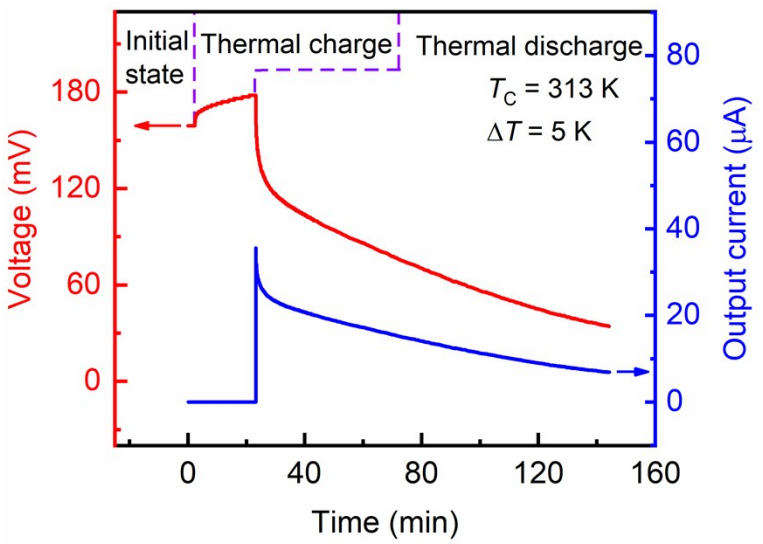

Fig. S37. Voltage and output current changes for i-TE-EC cells Gp | G-0.175/0.025 M $FeCN^{4-/3-}$ | Gp | G-0.10/0.05 M I^-/I_3^--0.4 M CF_3SO_3K | Gp in a continuous discharge at an external resistance of R = 5 kΩ.

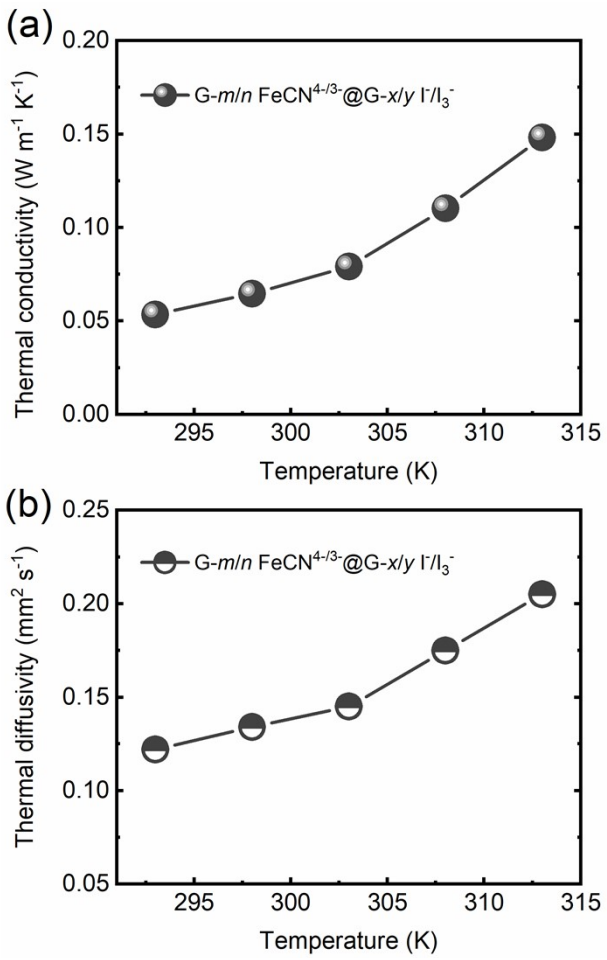

Fig. S38. Thermal properties of gel G-*m*/*n* $FeCN^{4-/3-}$@G-*x*/*y* I^-/I_3^- in a lamination condition. (a) Thermal conductivity and (b) thermal diffusivity with dependence of temperature at 293-313 K.

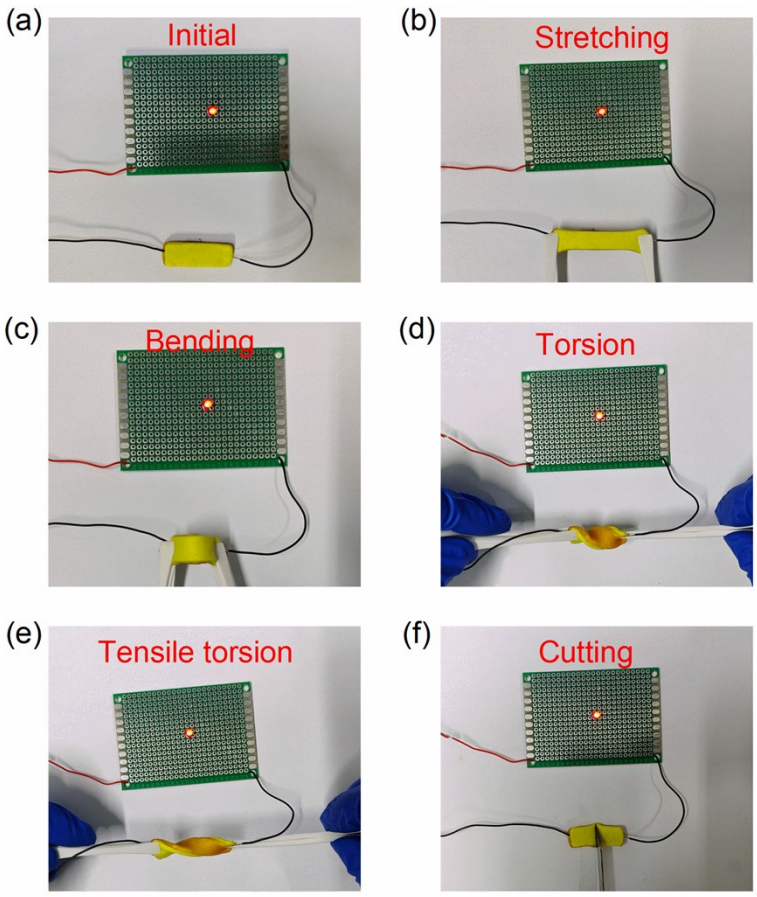

Fig. S39. The ability of conductivity for gels G-*m*/*n* $FeCN^{4-/3-}$, G-*x*/*y* I^-/I_3^-, and G-*m*/*n* $FeCN^{4-/3-}$|G-*x*/*y* I^-/I_3^- under different treatments. (a) Initial state, (b) Stretching, (c) Bending, (d) Torsion, (e) Tensile torsion, and (f) Cutting.

Table S1. Comparison of $P_{max}/(\Delta T)^2$ and output voltage (ΔT = 5 K) between i-TE-EC cell (this work) and reported i-TE cells.

Substances	Electrodes	S_i (mV K^{-1})	Voltage, $S_i \times \Delta T$ (mV)	$P_{max}/(\Delta T)^2$ (mW m^{-2} K^{-2})	Reference
G-$FeCN^{4-/3-}$ | G-I^-/I_3^--CF_3SO_3K	Graphite paper	-	176	10	This work
G-$FeCN^{4-/3-}$ | G-I^-/I_3^--CF_3SO_3K	Graphite paper; cation exchange membrane	-	224	20.5	This work
G-KCl-$FeCN^{4-/3-}$	Cu/Au	12.7	63.65	0.66	S3
PVA-CdmCl-$FeCN^{4-/3-}$	-	6.5	32.5	1.97	S4
Aqueous $FeCN^{4-/3-}$-NaOH	CNT buckypaper/aero gel sheet	1.4	7	2.5	S5
P(AM-co-AMPS)-$FeCN^{4-/3-}$-NaCl	-	1.65	8.25	0.61	S6
PAAm-phytic acid	carbon cloth/iron (II/III) phytate	26.7	133.5	20.26	S7
P(AA-AM)/CMC/H_2SO4	PANI@CWF	15	75	11.31	S8
Aqueous $FeCN^{4-/3-}$-UGdmCl	Graphite	4.2	21	1.1	S9
BC-$FeCN^{4-/3-}$-$Fe^{2+/3+}$	Cu sheets	4.53	22.65	0.03	S10
I^-/I_3^--MC-KCl	Graphite	9.62	48	0.358	S11
G-$FeCN^{4-/3-}$-Gr	Graphite paper/Au	13	65	1.03	S12
PAAm-SA-$FeCN^{4-/3-}$-CH_6ClN_3	Platinum wires	4.4	22	1.78	S13

*The corresponding full name for abbreviation in the table as follows.

G: gelatin

CNT: carbon nanotube

P(AM-co-AMPS): polymer (acrylamide and 2-acrylamide-2-methylpropane sulfonic acid)

PAAm: polyacrylamide

CMC: carboxymethyl cellulose

PANI@CWF: polymer redox polyaniline appended on the carbon weaved fabric

UGdmCl: urea and GdmCl

BC: bacterial cellulose

MC: methylcellulose

Gr: graphene

Table S2. The electrode temperature coefficient (α_R) for gels G-*m*/*n* $FeCN^{4-/3-}$ and G-*x*/*y* I^-/I_3^- in the temperature range of 293-333 K, Pt and saturated calomel electrode (SCE) used as the working electrode, reference and counter electrode, respectively.

Gels	Concentration (M)	Electrode temperature coefficient, α_R (mV K^{-1})
G-*m*/*n* $FeCN^{4-/3-}$	*m*/*n* = 0.05/0.35	-1.16
	m/*n* = 0.15/0.25	-1.35
	m/*n* = 0.25/0.15	-1.40
	m/*n* = 0.525/0.075	-1.46
	m/*n* = 0.35/0.05	-1.59
	m/*n* = 0.175/0.025	-1.56
G-*x*/*y* I^-/I_3^-	*x*/*y* = 0.10/0.05	0.65
	x/*y* = 0.20/0.10	0.67
	x/*y* = 0.40/0.20	0.67

Table S3. Comparison of energy density for i-TE cells in this work and the reported works.

Substances	Energy density ($J\ m^{-2}\ K^{-2}$)	Resistance (kΩ)	Electrode	Reference
G-$FeCN^{4-/3-}$ | G-I^-/I_3^--CF_3SO_3K	3.4	5	Graphite paper	This work
G-$FeCN^{4-/3-}$-Gr	0.19	2	Graphite paper/Au	S12
G-KCl-$FeCN^{4-/3-}$	0.37	3	3D-Cu/Au	S14
G-GTA/KCl-$FeCN^{4-/3-}$	0.99	3	Cu/Au	S15
PVA-$FeCN^{4-/3-}$	1.43	5	Au/Cr	S8

*The corresponding full name for abbreviation in the table as follows.

G: gelatin

Gr: graphene

GTA: glutaraldehyde

PVA: polyvinyl alcohol

Table S4. Comparison of $P_{max}/(\Delta T)^2$ for gels-device in this work and reports.

Substances	V_{OC} (V)	$P_{max}/(\Delta T)^2$ (mW m^{-2} K^{-2})	Cell number (n)	ΔT (K)	Electrode	Reference
G-$FeCN^{4-/3-}$ | G-I^-/I_3^--CF_3SO_3K	1.55	5.2	9	5	Graphite paper	This work
G-KCl-$FeCN^{4-/3-}$	2.2	0.08	25	10	Cu/Au	S3
PVA-$FeCN^{4-/3-}$	0.025	0.02	2	10	Au/Cr	S8
BC-$FeCN^{4-/3-}$	0.18	0.02	6	10	Cu sheets	S10
G-$FeCN^{4-/3-}$-Gr	0.12	1.17	4	3	Graphite/Au	S12
G-KCl-$FeCN^{4-/3-}$	2.8	0.28	24	10	3D-Cu/Au	S14
G-GTA/KCl-$FeCN^{4-/3-}$	3.6	0.50	16	12	Cu/Au	S15
PVA-$FeCN^{4-/3-}$	0.342	0.51	27	10	Pt wire	S16

*The corresponding full name for abbreviation in the table as follows.

G: gelatin

PVA: polyvinyl alcohol

Gr: graphene

BC: bacterial cellulose

GTA: glutaraldehyde

References

[S1] A. J. Debethune, T. S. Licht and N. Swendeman, *J. Electrochem. Soc*., 1959, **106**, 616.

[S2] G. Chen, Nanoscale Energy Transport and Conversion (Oxford Univ. Press, 2005).

[S3] C.-G. Han, X. Qian, Q. Li, B. Deng, Y. Zhu, Z. Han, W. Zhang, W. Wang, S.-P. Feng, G. Chen and W. Liu, *Science*, 2020, **368**, 1091–1098.

[S4] L. Liu, D. Zhang, P. Bai, Y. Mao, Q. Li, J. Guo, Y. Fang and R. Ma, *Adv. Mater.*, 2023, **35**, 2300696.

[S5] H. Im, T. Kim, H. Song, J. Choi, J. S. Park, R. Ovalle-Robles, H. D. Yang, K. D. Kihm, R. H. Baughman, H. H. Lee, T. J. Kang and Y. H. Kim, *Nat. Commun.*, 2016, **7**, 10600.

[S6] Z. Lei, W. Gao and P. Wu, *Joule*, 2021, **5**, 2211–2222.

[S7] W. Zhang, L. Qiu, Y. Lian, Y. Dai, S. Yin, C. Wu, Q. Wang, W. Zeng and X. Tao, *Adv. Sci.*, 2023, **10**, 2303407.

[S8] K. Jiang, J. Jia, Y. Chen, L. Li, C. Wu, P. Zhao, D. Y. Zhu and W. Zeng, *Adv. Energy Mater.*, 2023, **13**, 2204357.

[S9] J. Duan, G. Feng, B. Yu, J. Li, M. Chen, P. Yang, J. Feng, K. Liu and J. Zhou, *Nat. Commun.*, 2018, **9**, 5146.

[S10] Y. Zong, H. Li, X. Li, J. Lou, Q. Ding, Z. Liu, Y. Jiang and W. Han, *Chem. Eng. J.*, 2022, **433**, 134550.

[S11] Y. Han, J. Zhang, R. Hu and D. Y. Xu, *Sci. Adv.*, 2022, **8**, eabl5318.

[S12] C.-G. Han, Y. B. Zhu, L. Yang, J. Chen, S. Liu, H. Wang, Y. Ma, D. Han and L. Niu, *Energy Environ. Sci.*, 2024, **17**, 1559.

[S13] D. Zhang, Y. Mao, F. Ye, Q. Li, P. Bai, W. He and R. Ma, *Energy Environ. Sci.*, 2022, **15**, 2974–2982.

[S14] Y. Li, Q. Li, X. Zhang, B. Deng, C.-G. Han and W. Liu, *Adv. Energy Mater.*, 2022, **12**, 2103666.

[S15] Y. Li, Q. Li, X. Zhang, J. Zhang, S. Wang, L. Lai, K. Zhu and W. Liu, *Energy Environ. Sci.*, 2022, **15**, 5379–5390.

[S16] W. Gao, Z. Lei, W. Chen and Y. Chen, *ACS Nano*, 2022, **16**, 8347–8357.